Research Paper

Subwavelength Underwater Imaging of a Wire Array Metamaterial Based on Fabry-Pérot Resonance

Guo LI^{(1)*}, FeiLong LI⁽¹⁾, LiQing HU⁽²⁾, QunFeng LI⁽³⁾, GuanJun YIN⁽⁴⁾

(1) School of Automation, Xi'an Key Laboratory of Advanced Control and Intelligent Processing
Xi'an University of Posts and Telecommunications
Xi'an, China

(2) Electronic Materials Research Laboratory
Key Laboratory of the Ministry of Education and International Center for Dielectric Research
School of Electronic Science and Engineering, Xi'an Jiaotong University
Xi'an, China

(3) Jinan University Guangzhou, China

(4) Key Laboratory of Ultrasound of Shaanxi Province School of Physics and Information Technology, Shaanxi Normal University Xi'an, China

*Corresponding Author e-mail: liguo@xupt.edu.cn

Received May 20, 2025; revised October 7, 2025; accepted October 8, 2025; published online November 13, 2025.

Metamaterials with Fabry-Pérot (FP) resonance have proven effective for underwater ultrasound imaging. The propagation phenomenon can be understood as a spatial filter with linear dispersion over a finite bandwidth. However, conventional imaging techniques are constrained by the diffraction limit or rely on a strong impedance mismatch between the metamaterial and water. In this paper, we propose a columnar array metamaterial designed for underwater imaging based on FP resonances and validate the proposed design through numerical simulations. The acoustic pressure transmission coefficient, together with the normalized acoustic pressure distribution, is analyzed to quantitatively evaluate imaging quality and verify the physical effectiveness of the model. This novel structure enables deep subwavelength imaging underwater, maintaining excellent and stable imaging performance within a 0.4 kHz bandwidth centered around the operating frequency. We use air-filled metamaterials to create strong acoustic coupling and establish effective sound isolation. This approach significantly enhances imaging resolution, while optimizing energy loss at multiple interfaces, an issue in previous studies. Additionally, in contrast to resonance- or refraction-based approaches such as Helmholtz resonators or hyperlens designs, the proposed FP-resonant metamaterial offers an alternative mechanism for achieving near-field subwavelength imaging through controlled wave transmission and confinement. We also examine the influence of various parameters, such as imaging distance, incidence distance, and array periodicity, on imaging performance. The results demonstrate that the columnar array metamaterial holds great potential for underwater ultrasound imaging applications.

Keywords: Fabry–Pérot (FP) resonance; metamaterial underwater imaging; wire array metamaterial; air-filled metamaterials; finite element simulation.



1. Introduction

In recent years, the design and experimental realization of artificial metamaterials have yielded nu-

merous extraordinary physical properties (Dong et al., 2023; Kawata et al., 2008). The core purpose of acoustic metamaterials is to achieve precise control of sound wave propagation through artificially designed struc-

tures, breaking the physical limitations of natural materials, and thereby enabling acoustic functionalities that are unattainable with conventional materials at specific frequencies or in particular scenarios. A holeystructured metamaterial has demonstrated potential for near-field acoustic imaging beyond the diffraction limit, due to the strong coupling between the evanescent field components of a subwavelength object and the Fabry-Pérot (FP) resonances within the holes (Amireddy et al., 2017). However, the use of holeystructured metamaterial made from metals and polymers in underwater imaging faces significant challenges due to the low acoustic impedance mismatch and high viscous losses (Laureti et al., 2020; Astolfi et al., 2019; Estrada et al., 2008; Pendry, 2000; Chris-TENSEN et al., 2008; Belov, Silveirinha, 2006).

To address these limitations, we introduce the concept of a 'wire array' metamaterial, fabricated from a polymer with an acoustic impedance closely matching that of water. This design creates FP resonances within the array, while the air-filled gaps between the wires enhance acoustic isolation, enabling more efficient transmission of evanescent waves for deep-subwavelength underwater imaging (Molerón, Daraio, 2015). This approach paves a way for deep-subwavelength imaging using polymer-based acoustic metamaterials underwater (Gulia, Gupta, 2019; Deng et al., 2009).

It is well known that the resolution of traditional acoustic imaging devices is limited by the diffraction limit, which is half the operating wavelength, as these devices are unable to capture evanescent waves (Zhou et al., 2010; Yan, Yuan, 2015; Zhang et al., 2009; Ambati et al., 2008). These evanescent waves carry the fine details of objects but decay exponentially with distance (CHRISTENSEN, GARCÍA DE ABAJO, 2010). To achieve subwavelength resolution beyond the diffraction limit, hyperlenses and superlenses in artificial acoustic metamaterials have garnered significant attention by enhancing the transmission of evanescent waves (Amireddy et al., 2016; Simonet-TI, 2006). Hyperlenses are non-resonant, strongly anisotropic metamaterials that can convert evanescent waves into propagating waves (Liu et al., 2007; Guenneau et al., 2007; Silveirinha et al., 2008). In contrast, superlenses exhibit either single-negative or double-negative acoustic characteristics, achieved by using membrane-type metamaterials or Helmholtz resonators (LI, Chan, 2004). Superlenses achieve subwavelength resolution by reconstructing evanescent components through negative-index behavior, whereas Helmholtz-resonator designs utilize resonant enhancement of local acoustic fields to improve spatial confinement. Compared to these resonance- or refractionbased mechanisms, FP-resonant metamaterials offer a pathway to realize near-field imaging through controlling wave transmission and confinement within the structure. The effectiveness of holey-structured metamaterials has been demonstrated in air. In some instances, enhanced evanescent wave magnitude has been observed due to highly anisotropic equifrequency contours.

However, traditional metal materials struggle to create a strong impedance mismatch with water. To address this, ASTOLFI et al. (2019) employed tungsten in additive manufacturing to achieve a significant acoustic impedance mismatch with water, thereby improving the propagation of evanescent waves. Nonetheless, tungsten is challenging to process and it is quite heavy, making it inconvenient for underwater applications. Consequently, several holeystructured polymer-based metamaterials utilizing FP resonance have been proposed for subwavelength imaging (Liu et al., 2009). However, for underwater imaging with holey-structured metamaterials at higher frequencies, key challenges arise, including multimode coupling caused by weak acoustic impedance mismatch and high viscous losses between water and the metamaterial (LAFLEUR, SHIELDS, 1995; LAU-RETI et al., 2014; 2016). Underwater imaging with holey-structured metamaterials presents unique challenges. To address it, LAURETI et al. (2020) introduced the concept of using trapped air, where the acoustic impedance mismatch between a polymer and water is strongly enhanced when air is confined within the bulk material in a particular way. Additionally, the authors demonstrated that ultrasound imaging of broadband subwavelength apertures in water can be achieved using FP resonance. While these studies reported on polymer-based metamaterials functioning in water, acoustic coupling from the water-filled holes into the polymer is expected to degrade their performance (Laureti et al., 2020).

Recent advances have also explored alternative approaches to achieve subwavelength imaging beyond FP-based metamaterials. For example, neuralnetwork-assisted ultrasonic imaging methods, such as the back propagation neural network-total focusing method (BPNN-TFM), have demonstrated the ability to resolve defects separated by only 0.5λ , outperforming several existing super-resolution techniques (LIN et al., 2025). In the optical domain, semiconductor nanophotodetector (NPD) arrays, simulated with the multi-level multi-electron (MLME) finite-difference time-domain (FDTD) method, have achieved detection resolutions of about one-tenth of the operating wavelength, comparable to near-field scanning optical microscopy (Kim et al., 2008). These studies highlight the diversity of subwavelength imaging strategies across different physical platforms and provide a broader context for situating the present metamaterial-based approach, which offers a compact and efficient solution for underwater acoustic applications.

In this paper, we propose the use of polymers with acoustic impedance closely matched to that of water as columns in our metamaterial arrays. These arrays are surrounded by air and sealed with thin cover plates on both the front and back. The proposed design addresses the performance losses typically observed between water and polymers in traditional metamaterials, while it also eliminates efficiency reductions at the water-polymer-air interfaces found in trapped-air configurations. Furthermore, the significant impedance mismatch between the polymer and the surrounding air enhances the FP resonance. This design enables the minimum feature imaging size to be optimized to 0.12λ , compared to 0.135λ presented in the prior studies. Our findings demonstrate that these air-filled wire-array metamaterial exhibit outstanding imaging performance at deep subwavelength scales, along with a relatively broad bandwidth.

Through simulations, we optimized imaging frequency, distance, and incident conditions, and we also examined the effects of cover layer thickness and array periodicity on imaging quality. These insights offer valuable guidance for selecting material parameters. With the right configuration, the metamaterials can achieve optimal imaging performance and support potential practical applications. The proposed air-filled metamaterial design holds promise for several realworld applications that benefit from high-resolution underwater acoustic imaging. In the field of marine exploration, such a structure could be deployed for detailed seabed mapping and the detection of smallscale defects in underwater infrastructures. The ability to achieve subwavelength imaging in the near field allows fine structural details to be resolved, which are often blurred by the diffraction limit in conventional sonar systems. In addition, the approach is relevant to biomedical diagnostics in aqueous environments, such as high-frequency ultrasound imaging of tissues or monitoring of microscale biological processes. The strong impedance contrast between the water-like columns and the surrounding air provides efficient FP resonance, enabling enhanced focusing and improved image clarity. These capabilities suggest that the metamaterial design could serve as a compact, low-loss platform for next-generation acoustic microscopes or targeted biomedical sensing devices. Overall, positioning the proposed structure within such applicationoriented contexts highlights its potential impact beyond theoretical demonstration.

2. Structural designs

The FP resonance condition describes a scenario in which an acoustic wave undergoes repeated reflections between two parallel boundaries within a cavity, and constructive interference arises when the roundtrip propagation distance equals an integer multiple of the wavelength. Under this condition, acoustic energy becomes strongly confined within the cavity, resulting in resonance and enhanced transmission through the structure. In the context of acoustic metamaterials, this mechanism plays a critical role in amplifying evanescent components and thereby sustaining high-resolution imaging performance. By exploiting FP resonances, the metamaterial can overcome part of the diffraction limit and achieve subwavelength focusing or imaging in underwater environments.

Among the various sonic metamaterial designs, holey structures can achieve specific properties, such as extraordinary acoustic transmission or absorption. Previous studies have shown that, when diffraction effects can be neglected, the transmission process is primarily governed by the fundamental propagation modes within the holes. In this case, the zeroth-order transmission coefficient of an acoustic plane wave can be expressed as

$$t(\lambda, k) = \frac{4|S_0|^2 Y \exp(iq_z h)}{(1+Y|S_0|^2)^2 - (1-Y|S_0|^2)^2 \exp(2iq_z h)}, \quad (1)$$

where the parallel momentum $k = \sqrt{k_x^2 + k_y^2}$ and $q_z = k = 2\pi/\lambda$ is the propagation constant of the mentioned waveguide mode, $S_0 = a/A$ and $Y = k_0/\sqrt{k_0^2 - k^2}$ (ZHU et al., 2010). Objects positioned at the input surface of the holey plate can achieve near-perfect acoustic image transfer to the output side, owing to the plate's unique waveguiding properties. In this configuration, the transmission coefficients of both the transmitted and swift waves are unity. A simple analysis of a single hole in a structure with an infinite impedance mismatch with water predicts FP resonances at frequencies f_n , given by

$$f_n = N \frac{c}{2H},\tag{2}$$

where N is a positive integer representing the harmonic number, c is the speed of sound in water (1480 m/s), and H is the metamaterial thickness (the channel length) (LORENZO et al., 2021).

Previous studies have also interpreted the efficient transmission of subwavelength details in such structures through the concept of evanescent wave canalization, in which high spatial-frequency components are guided or transformed into propagating modes inside the metamaterial. This mechanism has been widely used to explain near-field image transfer in both acoustic and electromagnetic metamaterials.

However, these analyses typically rely on the examination of spatial frequency spectra, such as Fourier-domain representations or explicit separation between near-field and far-field contributions, to reveal how evanescent components are transmitted through the structure. In contrast, the present work focuses primarily on near-field imaging behavior, characterized by spatial pressure distributions, without performing a di-

rect decomposition of the field into its spatial frequency components. This approach emphasizes the practical imaging performance of the designed metamaterial, rather than the detailed modal evolution inside the structure.

In this paper, we introduce a new class of acoustic metamaterials designed for near-field underwater imaging applications. Figure 1 shows a typical structure, which consists of a soft wire array (easily penetrable by sound waves) with a width of $H = 50 \,\mathrm{mm}$. The array forms a periodic structure with a lattice parameter $A = 2 \,\mathrm{mm}$ (the distance between the centers of two adjacent arrays), and features deep-subwavelength square wires with a side length of $a = 1 \,\mathrm{mm}$. The gaps between wires in the array are filled with air, sealing the whole structure. This facilitates the generation of acoustic isolation and greatly enhances imaging quality (Belov et al., 2008; Astolfi et al., 2019). All the wires are arranged in parallel within a square hollow soft box, with front and rear cover thicknesses of $h = 0.5 \,\mathrm{mm}$ and wall thicknesses of $c = 2 \,\mathrm{mm}$. Both the soft wire array and the hollow structure are designed to be easily penetrable by underwater sound waves, using materials such as soft polymers. This metamaterial has an acoustic impedance closely matched to that of water, eliminating the traditional coupling losses caused by water-filled holes in polymer substrates, thereby improving imaging efficiency. In the simulations presented in this paper, the array and the metamaterial hollow cubic shell around the array are modeled with Young's modulus of 2400 MPa, a Poisson's ratio of 0.4, and a density of 1100 kg/m³. This 'wire array' metamaterial fabricated from polymers with acoustic impedance close to that of water, supports the formation of FP resonances inside the array, facilitating the transmission of evanescent waves and thus achieving subwavelength underwater imaging.

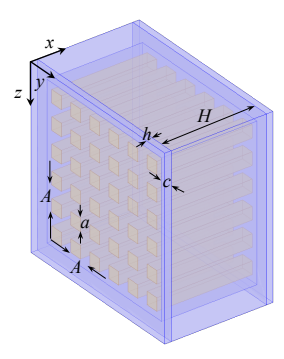


Fig. 1. Schematic diagram of a typical metamaterial structure.

It is worth noting that the acoustic impedance of the wires in array is close to that of water $(Z_{\text{polymer}} \approx Z_{\text{water}} = 1.48 \times 10^6 \, \text{Pa·s/m})$, and the acoustic impedance of air around the wire array $(Z_{\text{air}} = 411.6 \, \text{Pa·s/m})$ is very low. The evanescent waves scattered from the object under- water are confined within

each soft polymer wire, enhancing acoustic isolation due to the strong acoustic impedance mismatch between the polymer wire and air $\left(\frac{Z_{\text{polymer}}}{Z_{\text{air}}} \approx 3.6 \times 10^3\right)$. FP resonances occur in each individual polymer wire. Since the polymer arrays exhibit FP resonances under free boundary conditions in air, the significant impedance mismatch between the polymer wires and air ensures that viscous losses at the wire-air interface can be safely neglected during evanescent wave propagation in the metamaterial. The speed of sound and density are shown in Table 1.

Table 1. Material properties.

Material	Velocity [m/s]	Density [kg/m ³]	
Water	1500	1000	
Air	343	1.2	
Polymer	1477.1	1100	

3. Assumption of simulation

To enhance clarity and reproducibility, the key modeling assumptions adopted in this work are summarized further.

In this study, the interfaces between the front and back cover plates, the array columns, and the hollow outer shell are assumed to be perfectly bonded, without air gaps or leakage channels. This assumption is supported by practical fabrication processes, where robust bonding techniques generally ensure reliable sealing. Although minor imperfections may exist in practice, their effect on acoustic transmission is expected to be negligible compared to the dominant resonance and cavity–plate interactions.

The array columns are composed of metamaterial whose acoustic impedance closely matches that of water, while the surrounding regions are filled with air. This configuration minimizes interaction between the columns and the ambient medium, thereby suppressing unwanted scattering and allowing FP resonance to govern the system's response.

The side walls are modeled as acoustically hard boundaries, justified by their high stiffness and firm bonding to adjacent components, which render their vibrations negligible. In contrast, the thin front and back cover plates, directly exposed to the surrounding medium, are explicitly treated with acoustic—structure interaction, because their vibration significantly influences transmission.

All acoustic processes are considered linear, as the operating pressure levels are well below the thresholds for nonlinear effects such as harmonic generation, cavitation, or turbulence. Neglecting these effects avoids unnecessary computational complexity while preserving physical fidelity.

These assumptions are commonly adopted in acoustic metamaterial modeling and provide a balanced trade-off between physical realism and computational efficiency. While relaxing them might slightly alter quantitative metrics such as resonance amplitude or transmission efficiency, the essential FP resonance behavior and the associated imaging performance remain unaffected.

4. Simulation and results

To validate the subwavelength imaging capabilities of the wire array metamaterial, we conducted comprehensive 3D numerical simulations using COMSOL Multiphysics. The simulation was performed in the pressure acoustic-frequency domain, coupled with solid mechanics, to study the problem in detail. In the acoustic domain, we applied plane wave radiation conditions, sound absorption boundaries, and hard sound field boundaries. In the solid mechanics domain, constrained boundary conditions were set. We generated an acoustic-solid coupling boundary that encompasses the surfaces of the front and back covers of the metamaterial, as well as the perimeter of the array columns.

Our overall model construction is mainly divided into four parts, consisting of front-end water, metamaterial, back-end water, and perfectly matched layer (PML) (Fig. 2).

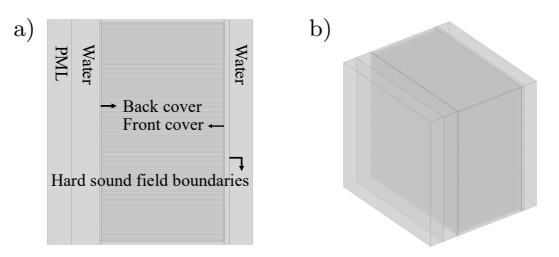


Fig. 2. a) Schematic of the simulation domain division; b) schematic of the full simulation model.

As described previously, the metamaterial array column is encapsulated within a hollow cubic shell, with both ends of the cube sealed by front and rear covers. The internal cavity of the cubic enclosure, excluding the space occupied by the array structure, is filled with air and maintained in a hermetically sealed condition. The front and rear cover thicknesses are defined as $0.5\,A$, where A is the period of the array. The side length of each square array column is denoted as a, the lateral (vertical) length of the array column is H, and the wall thickness of the surrounding hollow cubic shell is c.

We constructed an accurate simulation model to replicate a underwater environment for various test scenarios using COMSOL Multiphysics (Fig. 2), establishing the necessary theoretical conditions for the simulation. A plane wave is emitted, passes through the water, propagates to the metamaterial, generates resonance, and then forms an image on the opposite side. To ensure the simulation's accuracy, we included a PML (Fig. 2), beyond the water, with a wave

speed identical to that of water $(1480 \,\mathrm{m/s})$ to simulate an infinite domain. Additionally, impedance matching was applied around the metamaterial to ensure consistency and physical realism in the simulation.

To simulate plane wave emission for the image source, our approach is to first establish plane wave radiation conditions using a plane of the same size as the cover plate. As the sound wave propagates, we create a working plane of the same size as the plane wave emitting surface, referred to as 'E'. Outside the 'E' region, we apply hard acoustic field boundary conditions, while the area within the 'E' is left as a hollow space. This allows the acoustic wave to pass through the working plane and propagate toward the metamaterial surface. The 'E' structure consists of three horizontal rectangles, each measuring 46 mm in length and 6 mm in width, and one vertical rectangle measuring 62 mm in length and 6 mm in width, together forming the shape of the letter 'E' (hereafter referred to collectively as 'E').

This well-structured model is also facilitates precise mesh generation, resulting in concise calculations that meet the accuracy requirements for this work. We first applied swept meshing to the water domains and the PML, ensuring that the mesh size in the water region is less than $\lambda/6$, with the PML consisting of 20 layers, which complies with the established meshing criteria. Next, we applied mesh sweeps to the columns, the hollow metamaterial cubic shell, and the air domains within the metamaterials. The remaining connections between the front and rear cover plates were constructed using a free tetrahedral mesh. We conducted a grid convergence study by refining the mesh until the resonant frequency variation was below 0.05 %. In addition, we verified the numerical stability by adjusting solver tolerance and frequency step size, both of which showed negligible influence on the results.

Additionally, to better evaluate the imaging performance on the receiving surface, we analyzed the sound pressure distribution along a 3D cut line (Fig. 3). This allowed us to observe the variation trends in sound pressure. As illustrated, the 3D cut line lies along the yz-plane at the intended focal distance, positioned at the center of the hollow 'E' structure on the working plane, thereby encompassing its three horizontal edges. The vertical axis spans from 0 m (near the lower edge) to $0.092\,\mathrm{m}$ (near the upper edge). By examining the sound pressure distribution along this line, we can assess the imaging quality. An optimal focusing effect should exhibit the following characteristics:

- 1) a smooth and continuous pressure profile,
- 2) peak sound pressure at the three edges of the 'E'
- 3) minimum sound pressure in the regions between the adjacent edges,
- 4) approximately uniform sound pressure magnitudes across all three edges.

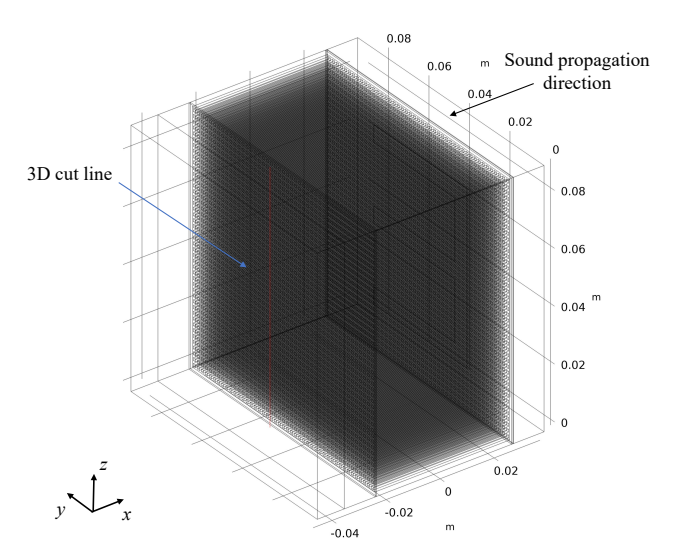


Fig. 3. 3D cut line.

In this model, since the sound wave propagates in the negative x-direction, the sound pressure value obtained on the imaging plane is inherently negative. Therefore, the absolute sound pressure value should be used for comparative analysis of the sound pressure magnitude.

Before initiating the simulation test groups, we measured the acoustic pressure transmission coefficient of the material. The sound source setup is identical to the one presented the previous section: a plane wave is emitted from the rightmost plane, passing through the hollow 'E' to reach the front cover of the metamaterial. The output face is defined as the end face of the cover farthest from the sound source, from which we extract the total acoustic pressure $(P_{\rm out})$. The input face, closer to the sound source, is used to extract the total acoustic pressure $(P_{\rm in})$. The sound pressure transmission coefficient is calculated as the ratio of $P_{\rm out}$ to $P_{\rm in}$. We selected a frequency range of 27 kHz to 34 kHz and plotted the sound pressure transmis-

sion coefficient curve, as shown in Fig. 4. From the curve, we observe that the transmission coefficient exceeds 0.82 within the frequency range of 30.6 kHz to 31.6 kHz, maintaining a broad bandwidth. This information is crucial for identifying the optimal incidence frequency. However, there may be a slight deviation between this frequency range and the actual frequency that yields the highest imaging quality.

The preceding analysis of the acoustic pressure transmission coefficient $(P_{\text{out}}/P_{\text{in}})$ provides a quantitative, physics-based measure of the metamaterial's ability to transmit both propagating and evanescent components. In principle, more detailed metrics such as the point-spread function (PSF) or modulation transfer function (MTF) could be extracted from full-wave simulations using tools such as the finite-difference timedomain (FDTD) or transfer matrix method (TMM), which compute the response to different transverse wave vectors $(\mathbf{k}_x, \mathbf{k}_y)$ (ZHU et al., 2018). The $P_{\text{out}}/P_{\text{in}}$ analysis employed here captures the essential physics of energy transmission and validates the effectiveness of the overall model, providing a simplified yet rigorous basis for subsequent visual evaluation of near-field subwavelength imaging performance.

4.1. Optimal imaging frequency comparison

To determine the optimal imaging frequency, the incident frequency was first varied, revealing a range between $27.5\,\mathrm{kHz}$ and $30\,\mathrm{kHz}$ in which clear imaging was achievable. A step size of $0.1\,\mathrm{kHz}$ was used for a frequency sweep. For these simulations, the imaging distance of $1.5\,A$ and the incident distance of $0.1\,A$ were tentatively set. The corresponding visual imaging results are shown in Fig. 5, and the quantitative sound pressure distributions across the image plane for selected frequencies are shown in Fig. 7.

As shown in Figs. 5 and 6, we observed that imaging quality is poor between 27.5 kHz to 28.5 kHz,

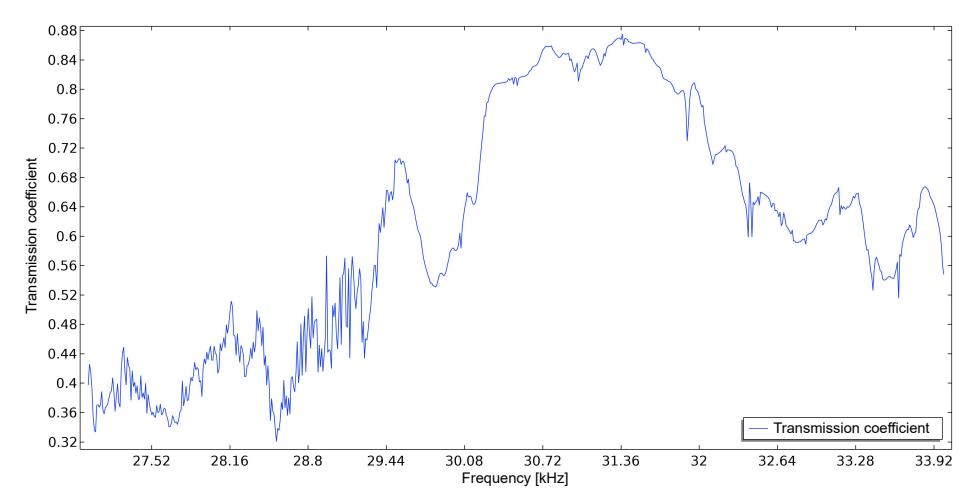


Fig. 4. Transmission coefficient range from $27\,\mathrm{kHz}$ to $34.0\,\mathrm{kHz}$.

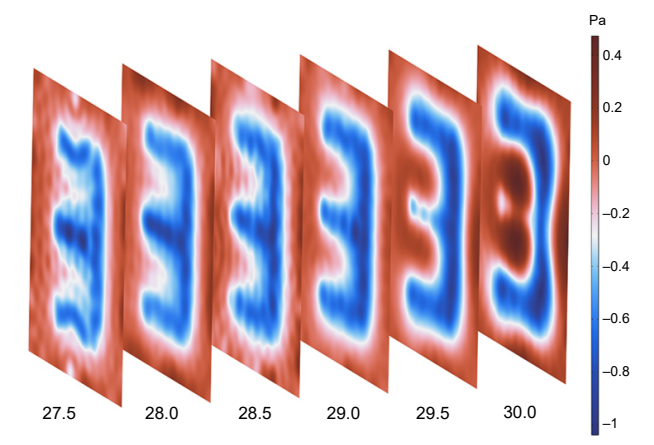


Fig. 5. Overall imaging frequency range from 27.5 kHz to 30.0 kHz.

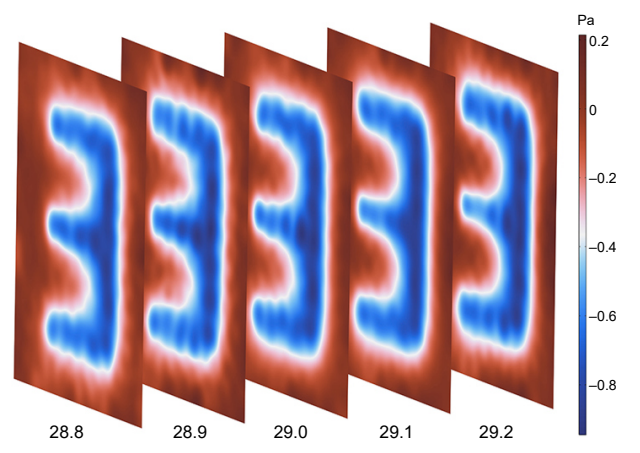


Fig. 6. Optimal imaging frequency range from 28.8 kHz to 29.2 kHz.

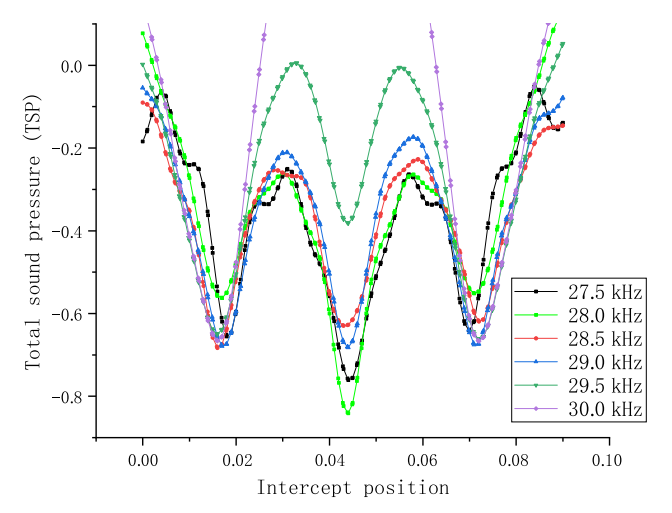


Fig. 7. Sound pressure curves in the frequency range of 27.5 kHz to 30.0 kHz.

the sound pressure distribution along the three boundaries of the 'E' is uneven, and fine details are not well presented. Additionally, at the vertical junctions, defocusing occurs, resulting in an unclear outline of the object. When the frequency exceeds 29.2 kHz, a no-

ticeable thinning occurs at the center of the image 'E', which does not satisfy our imaging quality requirements. In contrast, Fig. 6 shows the optimal imaging frequency range from 28.8 kHz to 29.2 kHz, where these issues are resolved.

In the 29.5 kHz-30 kHz image, the second side of the 'E' is not well imaged, the outline of the image 'E' improves, though some intermittent areas remain. It can be seen from the sound pressure curve in Fig. 7 that, consistent with our imaging effect, the 27.5 kHz sound pressure curve is not smooth near the 0.03 mm and 0.06 mm positions. The reason is that there is defocusing at the boundary, and the background field sound pressure and the transmitted sound pressure cannot be distinguished well. This situation results in poor presentation of image detail information. The sound pressure transmission at the lowest peak of the 28 kHz sound pressure curve, which is the second side of 'E', is good, but the sound pressure transmission at the other two sides (the first and third lowest peaks) differs and cannot be transmitted very evenly, which caused the center of the 'E' to be clearly imaged while the surrounding areas appear blurred.

At 28.5 kHz, the curve is very smooth as a whole, smooth at the position of 0.03 mm and 0.06 mm positions of the sound pressure curve section, and the sound pressure at the three lowest peaks is nearly equal. However, the 29 kHz curve shows higher transmission sound pressure and a larger difference between the maximum and minimum peaks, resulting in better imaging quality. At 29.5 kHz curve, the absolute value of the sound pressure at the second minimum point is smaller than the transmission sound pressure at the other two sides, that is, the resolution effect of the second side of the 'E' is poor. At 30 kHz, the sound pressure on the second side is not less than 0, so the second side of the 'E' is almost invisible. After comparison, we determined that the optimal imaging frequency lies between 28.8 kHz and 29.2 kHz (Fig. 6). This frequency range demonstrates good imaging quality and robustness.

Comparing the sound pressure curves in Fig. 8, it is found that within the frequency range of 28.8 kHz to 29.2 kHz, the sound pressure curves are very smooth and the imaging effect is good, but there is a slight difference between the minimum and maximum peaks. At 29 kHz, the transmission sound pressure values at the three minimum peaks of the curve are closer. In addition, there is a large difference between them and the maximum peak, enabling better distinction of the image details. The imaging effect at 29.2 kHz is inferior to that at 29 kHz because the absolute value of the sound pressure of the second side of the 'E' is lower. Consequently, we selected 29 kHz as the optimal frequency for subsequent analyses. The imaging quality across the frequency range is summarized in Table 2.

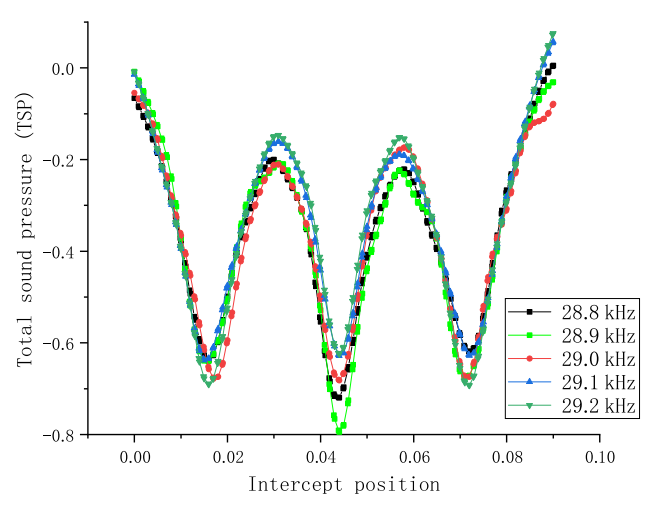


Fig. 8. Sound pressure curves in the frequency range of 28.8 kHz to 29.2 kHz.

Table 2. Imaging quality under different incident frequencies.

Frequency range [kHz]	Imaging quality	Main features / issues
27.5–28.5	Poor	Uneven sound pressure; defocusing at junctions; poor details
28.8–29.2	Good	Smooth curves; balanced transmission across edges; robust imaging
29.2–30.0	Degraded	Central thinning, edge degradation; second edge fades at 30 kHz

4.2. Comparison of optimal imaging distance

After establishing the incident frequency at $29\,\mathrm{kHz}$, we proceeded to determine the optimal imaging distance. During this phase, the distance from the 'E' sound-emitting surface to the front cover plate of the metamaterial was fixed at $0.1\,A$, while all other parameters were kept constant. Cross-sections were generated at intervals ranging from from $0.1\,A$ to $3\,A$ to adjust the receiving surface and obtain the corresponding images (Fig. 9).

As shown in Fig. 9, the imaging distance has a significant impact on image quality. At $0.1\,A$, the imaging surface is closest to the cover plate, where the sound pressure distribution is relatively uniform and the outline of the 'E' is clear, with minimal edge defocusing. This results in a more realistic reconstruction. As the imaging distance increases, the absolute sound pressure on the three sides of the 'E' decreases markedly, the contrast with the background weakens, and junction details become blurred. This degradation arises from evanescent wave decay: high-frequency spatial Fourier components $(k_z > k_0)$ diminish exponentially

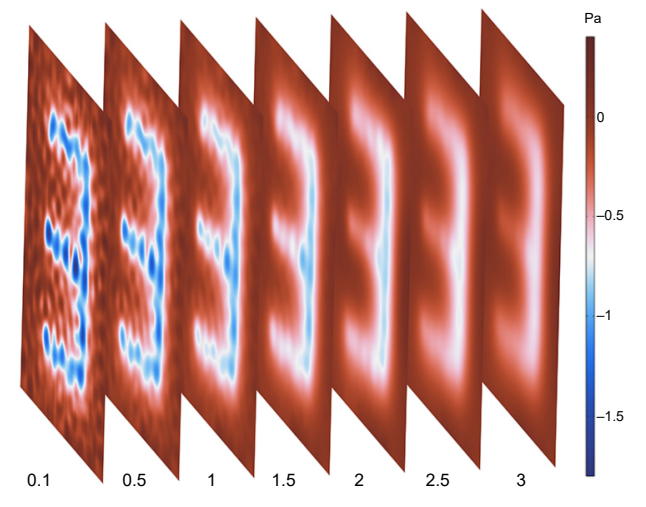


Fig. 9. Imaging performance comparison from $0.1\,A$ to $3\,A$ for optimal distance selection.

with distance $e^{-|k_z|z}$, leading to the loss of subwavelength information.

The sound pressure curves in Fig. 10 further validate these observations. At 0.1 A, the transmitted sound pressure of the three sides of the 'E' reaches its maximum, with noticeable peaks and stronger contrast between maxima and minima, which enhances detail resolution despite some extra oscillations. With increasing distance, the curves become smoother and extra peaks disappear, but the difference between the highest and lowest values diminishes, reducing image sharpness. Moreover, the peak distribution indicates that the second side of the 'E' is imaged more clearly than the upper and lower sides, leading to uneven reconstruction. Although small oscillations remain at 0.1 A, these can be mitigated using filtering or curve-fitting algorithms (Allen, Vlahopoulos, 2002). Based on these results, the optimal imaging distance was determined to be 0.1 A. The imaging performance at different distances is summarized in Table 3.

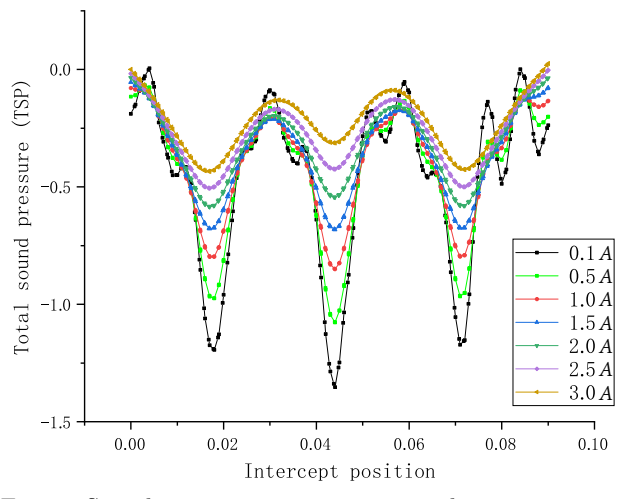


Fig. 10. Sound pressure curves at imaging distances ranging from $0.1\,A$ to $3\,A$.

Imaging distance (A)	Imaging quality	Main features / issues
0.1	Good	Clear outline; uniform sound pressure; minimal defocusing
0.5–1	Medium	Reduced contrast; partial blurring at junctions;

uneven side imaging

Significant loss of detail;

weak contrast with background

due to evanescent wave decay

Table 3. Summary of imaging performance at different distances.

4.3. Comparison of optimal incidence distances

>1

Poor

Through comparative simulations, we established that the optimal incident frequency is $29\,\mathrm{kHz}$ and the best receiving distance is $0.1\,A$. Based on these parameters, we further analyzed the influence of incident distance to determine a more suitable configuration. During this process, the receiving plane was fixed at $0.1\,A$ from the back cover plate of the metamaterial, while the incident plane was adjusted from $0.1\,A$ to $3\,A$ (Fig. 11). The model parameters and meshing were independently recalculated for each distance, while the acoustic boundary conditions remained consistent with the default boundary around the 'E'.

As shown in Fig. 11, the imaging quality degrades progressively as the incident distance increases. When the incident distance is $0.1\,A$, the 'E' image is sharp and continuous, with a uniform sound pressure distribution and minimal edge distortion. The short propagation distance enhances evanescent wave coupling,

resulting in strong transmitted sound pressure and a clear reconstruction of all edges. As the incident distance increases to $0.3\,A-0.5\,A$, the transmitted sound pressure along the three edges of the 'E' decreases, accompanied by the emergence of stray peaks and mild distortion in the image. At $1\,A$, the central region of the sound field becomes dominant, while the upper and lower edges weaken, causing the 'E' to appear blurred. When the incident distance further increases to $2\,A-3\,A$, the image of the 'E' becomes indistinct and nearly disappears.

The sound pressure curves in Fig. 12 confirm this trend. The decrease in transmitted sound pressure amplitude and the growing smoothness of the curves reflect the attenuation of high-frequency evanescent components. Additionally, slight impedance mismatches

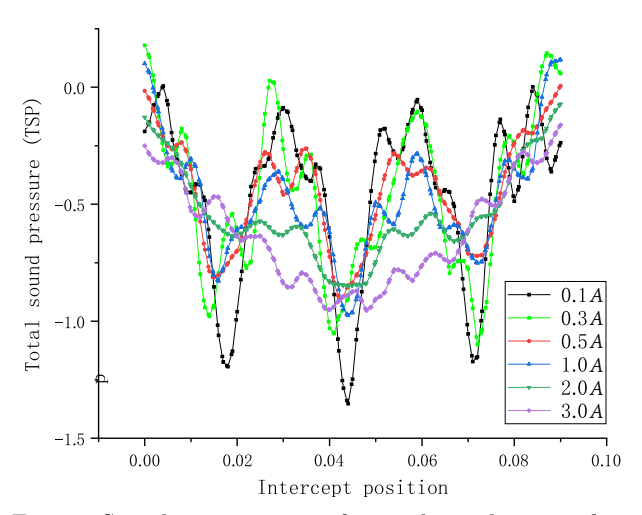


Fig. 12. Sound pressure curve for incidence distances from $0.1\,A$ to $3\,A$.

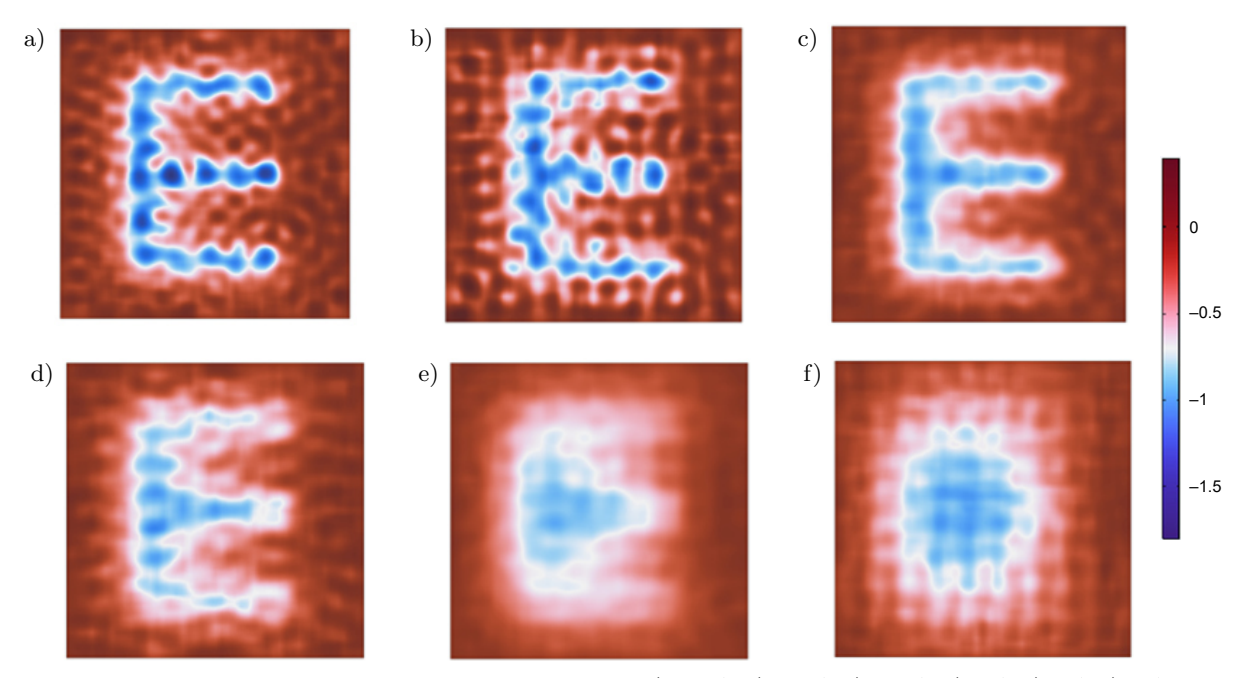


Fig. 11. Comparison of optimal incidence distances: a) 0.1 A; b) 0.3 A; c) 0.5 A; d) 1 A; e) 2 A; f) 3 A.

between the metamaterial covers and water cause multiple reflections between the 'E' baffle and the front cover, introducing stray peaks and positional shifts in the sound pressure extrema. These effects lead to degradation of subwavelength imaging performance. To preserve high-frequency information and minimize wave interference, the incident plane should be positioned as close as possible to the metamaterial surface. Consequently, $0.1\,A$ is determined to be the optimal incident distance. The imaging performance at different incident distances is summarized in Table 4.

Table 4. Summary of imaging performance at different incident distances.

Imaging distance (A)	Imaging quality	Main features / issues
0.1	Good	Strong evanescent coupling; uniform sound pressure; minimal edge distortion
0.3-0.5	Medium	Slight loss of edge sharpness; reduced sound pressure; appearance of stray peaks
1.0	Poor	Central sound field dominates; weakened upper/lower edges; image blurring
2.0-3.0	Very Poor	Strong reflection effects; severe evanescent decay; 'E' shape almost invisible

4.4. Comparison of imaging quality after changing cover thickness

As previously established, the optimal incident frequency is 29 kHz, and both the optimal receiving and

incident distances are set to $0.1\,A$. In the following analysis, the thickness of the metamaterial's front and back cover plates was varied simultaneously from $0.5\,\mathrm{mm}$ to $3.0\,\mathrm{mm}$ to examine its influence on imaging quality, while maintaining the optimal geometric and acoustic conditions. To ensure accurate comparison, the water region length in the model was kept constant during all simulations.

As illustrated in Fig. 13, increasing the cover plate thickness leads to a gradual degradation of imaging quality. When the thickness is 0.5 mm, the imaging of the letter 'E' is clear and continuous, indicating good acoustic transmission and minimal phase distortion. As the thickness increases to around 1.0 mm-1.5 mm, slight blurring and burrs appear along the middle horizontal stroke of the 'E', and local discontinuities emerge due to partial phase mismatching between the transmitted and reflected sound waves. At 2.0 mm, the central line of the 'E' exhibits breakpoints, and at 3.0 mm, both the upper and lower horizontal edges begin to curve and distort, with the overall image becoming defocused and noisy. This degradation is primarily attributed to the multiple reflections within the thicker cover layers, which induce phase interference and attenuate the effective transmission of evanescent components.

The sound pressure trends in Fig. 14 further validate this observation. When the cover plate is thin (0.5 mm), the transmitted acoustic pressure along the three edges of the 'E' reaches higher absolute values and shows clear separation between peaks and troughs, corresponding to sharp and distinct image boundaries. With increasing thickness, the sound pressure

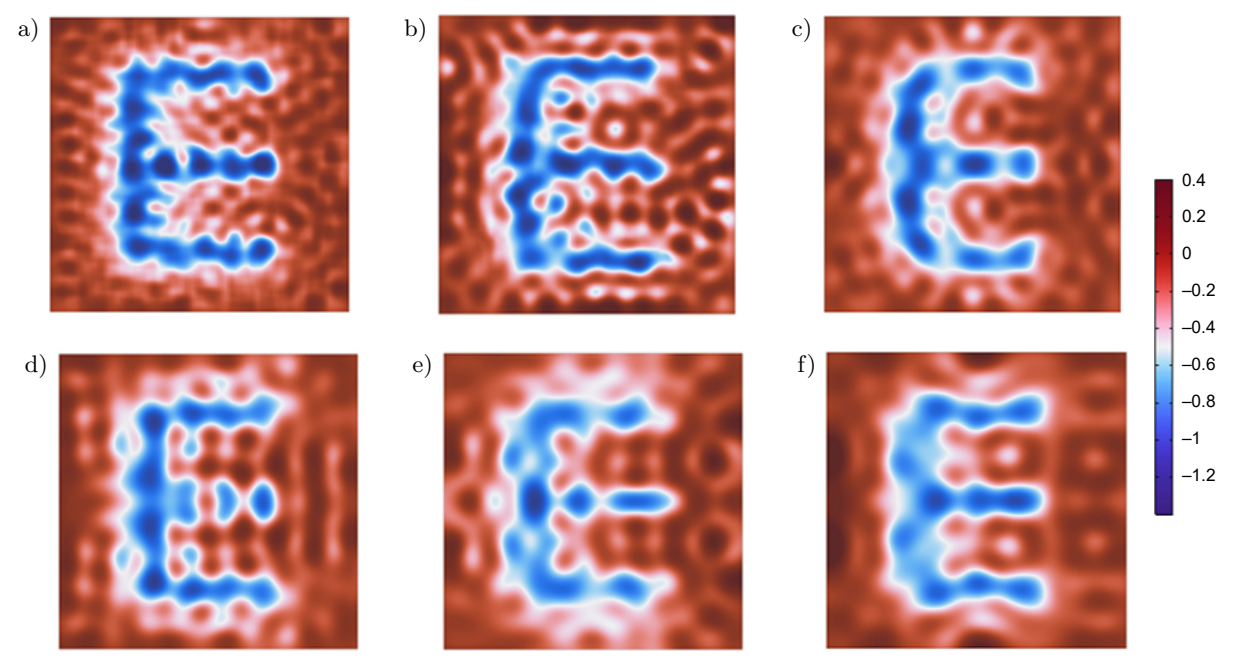


Fig. 13. Comparison of imaging quality for different cover thickness: a) 0.5 mm; b) 1.0 mm; c) 1.5 mm; d) 2.0 mm; e) 2.5 mm; f) 3.0 mm.

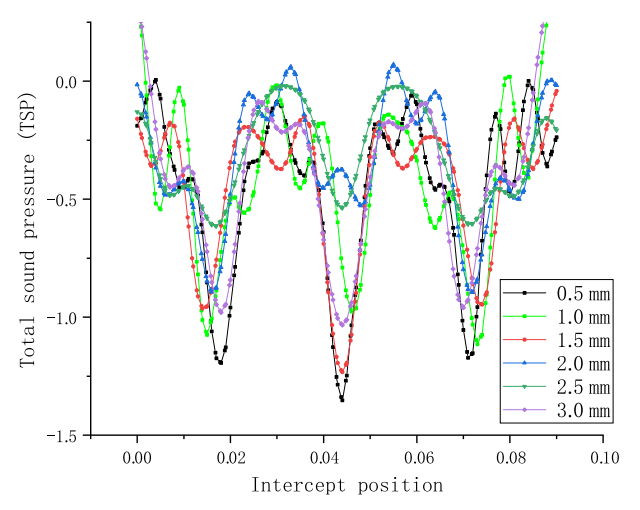


Fig. 14. Sound pressure curves for cover thicknesses ranging from $0.5\,\mathrm{mm}$ to $3.0\,\mathrm{mm}$.

curves become progressively irregular, with more spurious peaks and reduced amplitude differences, indicating uneven transmission and increased scattering within the covers. At 2.0 mm and beyond, the pressure at the second edge of the 'E' weakens sharply, while background pressure fluctuations intensify, causing image details to blur or disappear.

In summary, increasing the cover plate thickness results in stronger internal reflection and enhanced evanescent decay, leading to phase distortion and reduced subwavelength imaging fidelity. The 0.5 mm cover thickness provides the most stable and clear imaging performance under the given conditions.

4.5. Comparison of imaging quality with changing array cycles

The aim of this experiment is to maintain the size and position of the letter 'E' while proportionally reducing both the column bottom edge length (a) and the array period, ensuring that their ratio to the original model remains constant. In the original configuration, each edge of the 'E' corresponds to the orthocenter between two arrays. After scaling down, it is crucial to preserve the alignment of the 'E' with this orthocenter. However, if the dimensions of the 'E' remain unchanged, precise alignment of all three edges with the intended array positions cannot be guaranteed. Therefore, the dimensions of the 'E' are finetuned to ensure full alignment with the adjusted array configuration. Throughout this process, both the incidence and reception distances are maintained at their optimal values, and the cover plate thickness is fixed at 0.5 mm to achieve the best imaging performance.

As shown in Fig. 15, the comparison across six sets of experiments reveals that when only a single column exists within the gap of the 'E', the resulting image appears blurred, and the 'E' is indistinguishable at the optimal imaging distance. With two columns, imaging quality improves but remains suboptimal. When the number of columns increases to three, the 'E' becomes distinctly visible, and its outline more closely resembles that of the model at the incident plane. At four columns, the image contours are clearer, with straighter sides and nearly perpendicular intersections, further enhancing fidelity to the original 'E'. However, as the number of columns increases to five and six,

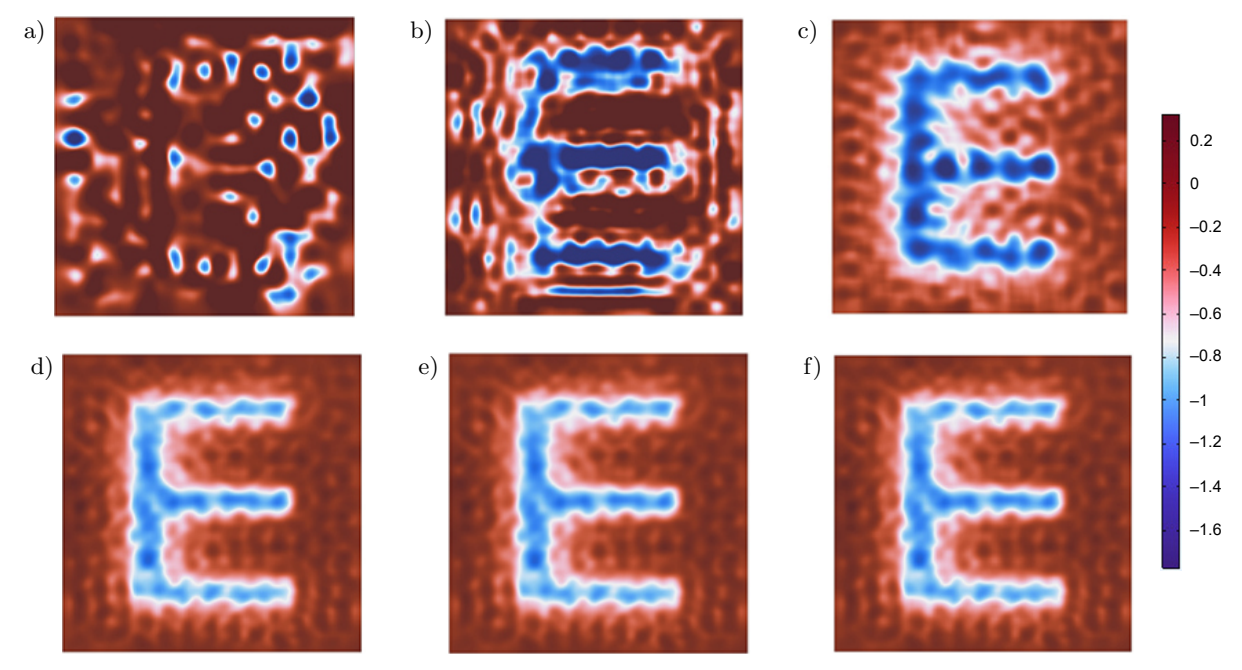


Fig. 15. Comparison of imaging quality with varying number of array columns: a) 1; b) 2; c) 3; d) 4; e) 5; f) 6.

no substantial improvement is observed, indicating that image quality reaches saturation at four columns.

From the sound pressure distributions shown in Fig. 16, imaging with a single column is ineffective; hence, analysis begins with two columns. When two array columns are used, the absolute acoustic pressure along the three edges of the 'E' is high, and the contrast with the background field is pronounced. However, numerous spurious peaks appear, and the background field is irregular. When the number of columns increases to three, the absolute pressure at the 'E' edges slightly decreases, but the background field becomes more uniform. With four or more columns, the sound pressure curves show minimal further change. Although the absolute pressure at the edges continues to decrease slightly, the background field remains evenly distributed, resulting in a stable and clearly defined image.

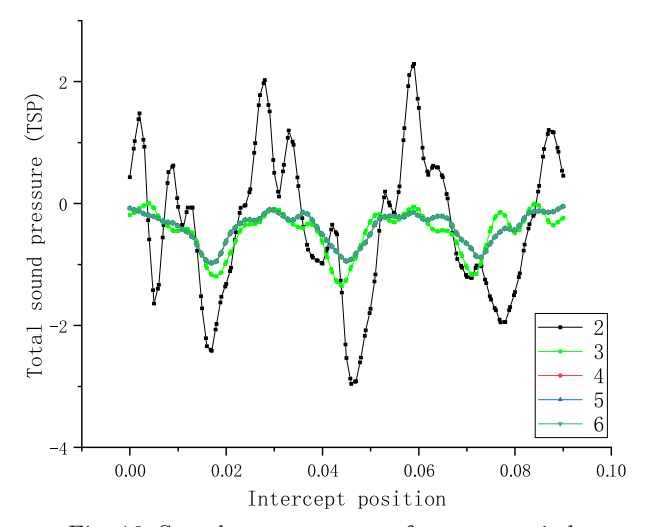


Fig. 16. Sound pressure curves for array periods corresponding to 2 to 6 columns.

It is worth noting that these imaging results were obtained under idealized simulation conditions, without considering real-world disturbances such as background acoustic noise, medium inhomogeneity, or object motion, which are common in underwater environments. Although this simplification enables a clear evaluation of the intrinsic imaging performance of the proposed metamaterial, future work will incorporate these factors to assess the robustness and practical applicability of the system under realistic underwater conditions.

5. Conclusions

This work demonstrated that by placing the image plane at a specific distance from the output plane, a faithful representation of the 'E' pattern underwater can be achieved. The imaging quality is influenced by several factors, including incident frequency, incident

distance, imaging distance, cover thickness, and array period. By adjusting the frequency, we can achieve high-quality imaging within the range of 28.8 kHz to 29.2 kHz, with an optimum frequency of 29 kHz, indicating that the metamaterial exhibits a broad bandwidth response. We determined the optimal incidence and imaging distances to be 0.2 mm from both the front and rear cover plates.

Additionally, we found that excessive cover thickness negatively impacts imaging quality, with the optimal thickness being 0.5 mm. Furthermore, we confirmed that the array period plays a significant role in enhancing imaging quality. As the number of arrays passing through the 'E' increases, the imaging quality improves; however, when more than four array columns are present, the quality tends to saturate and does not significantly change with the addition of more columns. These findings confirm that a wire array metamaterial functions effectively as a near-field acoustic imaging device capable of operating at very deep subwavelength scales underwater. This imaging capability and the associated principles provide some theoretical support for applications, including medical ultrasonography, micro-device flaw detection, and ultrasonic non-destructive evaluation.

Competing interests

The authors declare that they have no known competing financial interests or personal relationships that could have appeared to influence the work reported in this paper.

Fundings

This work was supported by the National Natural Science Foundation of China (no. 12104369, 12174004), the Postgraduate Innovation Project Fund of Xi'an University of Posts and Telecommunications (CXJJZL2023032), the State Key Laboratory for Manufacturing Systems Engineering open fund (no. sklms2022001), the general grant of Shaanxi Province in China (no. 2023-JC-YB-521), the Zhuhai City Philosophy and Social Sciences Planning 2023 Annual Planning Project (2023YBB054, GD23XTY35), and the Guangdong Province Philosophy and Social Sciences Planning 2023 Discipline Co-construction Project (GD23XTY35).

AUTHORS' CONTRIBUTIONS

Guo Li was responsible for conceptualization, funding acquisition, resources, supervision, writing original draft; FeiLong Li was responsible for data curation, investigation, methodology, formal analysis, finite element simulation, writing original draft; LiQing Hu was responsible for finite element simulation, investigation; QunFeng Li was responsible for resources, supervision;

GuanJun Yin was responsible for finite element simulation, validation. All authors reviewed and approved the final manuscript.

References

- Allen M.J., Vlahopoulos N. (2002), Numerical probabilistic analysis of structural/acoustic systems*, Mechanics of Structures and Machines, 30(3): 353– 380, https://doi.org/10.1081/SME-120004422.
- Ambati M., Fang N., Sun C., Zhang X., (2008), Surface resonant states and superlensing in acoustic metamaterials, *Physical Review B*, 75(19): 195447, https://doi.org/10.1103/PhysRevB.75.195447.
- Amireddy K.K., Balasubramaniam K., Rajago-Pal P. (2016), Holey-structured metamaterial lens for subwavelength resolution in ultrasonic characterization of metallic components, *Applied Physics Letters*, 108(22): 224101, https://doi.org/10.1063/1.4950967.
- 4. Amireddy K.K., Balasubramaniam K., Rajago-Pal P. (2017), Deep subwavelength ultrasonic imaging using optimized holey structured metamaterials, *Scien*tific Reports, **7**: 7777, https://doi.org/10.1038/s41598-017-08036-4.
- ASTOLFI L. et al. (2019), Negative refraction in conventional and additively manufactured phononic crystals, [in:] 2019 IEEE International Ultrasonics Symposium (IUS), pp. 2529–2532, https://doi.org/10.1109/ULT SYM.2019.8926236.
- Belov P.A., Silveirinha M.G. (2006), Resolution of subwavelength transmission devices formed by a wire medium, *Physical Review E*, 73(5): 056607, https://doi.org/10.1103/PhysRevE.73.056607.
- Belov P.A., Silveirinha M.G., Simovski C.R., Hao Y., Parini C. (2008), Comment on "Guiding, Focusing, and Sensing on the Subwavelength Scale Using Metallic Wire Arrays", arXiv, https://doi.org/ 10.48550/arXiv.0804.3670.
- CHRISTENSEN J., MARTIN-MORENO L., GARCIA-VIDAL F.J. (2008), Theory of resonant acoustic transmission through subwavelength apertures, *Physical Review Letters*, 101(1): 014301, https://doi.org/10.1103/PhysRevLett.101.014301.
- CHRISTENSEN J., GARCÍA DE ABAJO F.J. (2010), Acoustic field enhancement and subwavelength imaging by coupling to slab waveguide modes, *Aplied Physics Letters*, 97(16): 164103, https://doi.org/10.1063/1.3504700.
- Deng K., Ding Y., He Z., Zhao H., Shi J., Liu Z. (2009), Theoretical study of subwavelength imaging by acoustic metamaterial slabs, *Journal of Applied Physics*, 105(12): 124909, https://doi.org/10.1063/1.3153976.
- Dong E., Cao P., Zhang J., Zhang S., Fang N.X., Zhang Y. (2023), Underwater acoustic metamaterials, National Science Review, 10(6): 258–280, https://doi.org/10.1093/nsr/nwac246.

- 12. ESTRADA H., CANDELAS P., URIS A., BELMAR F., GARCÍA DE ABAJO F.J., MESEGUER F. (2008), Extraordinary sound screening in perforated plates, *Physical Review Letters*, **101**(8): 084302, https://doi.org/10.1103/PhysRevLett.101.08430.
- GUENNEAU S., MOVCHAN A., PÉTURSSON G., RA-MAKRISHNA S.A. (2007), Acoustic metamaterials for sound focusing and confinement, New Journal of Physics, 9: 399, https://doi.org/10.1088/1367-2630/9/11/399.
- 14. Gulia P., Gupta A. (2019), Sound attenuation in triple panel using locally resonant sonic crystal and porous material, *Applied Acoustics*, **156**: 113–119, https://doi.org/10.1016/j.apacoust.2019.07.012.
- KAWATA S., ONO A., VERMA P. (2008), Subwavelength colour imaging with a metallic nanolens, *Nature Pho*tonics, 2(7): 438–442, https://doi.org/10.1038/npho ton.2008.103.
- KIM K.Y., LIU B., HUANG Y., HO S.-T. (2008), Simulation of photodetection using finite-difference time-domain method with application to near-field subwavelength imaging based on nanoscale semiconductor photodetector array, *Optical and Quantum Electronics*, 40(5): 343–347, https://doi.org/10.1007/s11082-008-9190-0.
- 17. Lafleur L.D., Shields F.D. (1995), Low-frequency propagation modes in a liquid-filled elastic tube waveguide, *The Journal of the Acoustical Society of America*, **97**(3): 1435–1445, https://doi.org/10.1121/1.412981.
- LAURETI S., DAVIS L.A.J., RICCI M., HUTCHINS D.A. (2014), The study of broadband acoustic metamaterials in air, [in:] 2014 IEEE International Ultrasonics Symposium, pp. 1344–1347, https://doi.org/10.1109/ULTSYM.2014.0332.
- LAURETI S. et al. (2020), Trapped air metamaterial concept for ultrasonic subwavelength imaging in water, Scientific Reports, 10(1): 10601, https://doi.org/ 10.1038/s41598-020-67454-z.
- LAURETI S., HUTCHINS D.A., DAVIS L.A.J., LEIGH S.J., RICCI M. (2016), High-resolution acoustic imaging at low frequencies using 3D-printed metamaterials, *American Institute of Physics Advances*, 6(12): 121701, https://doi.org/10.1063/1.4968606.
- 21. Li J., Chan C.T. (2004), Double-negative acoustic metamaterial, *Physics Review E*, **70**(5): 055602, https://doi.org/10.1103/PhysRevE.70.055602.
- Lin L., Shen H., Shi S., Zhang D., Fu D., Ma Z. (2025), Subwavelength resolution imaging of ultrasonic total focusing method by decoupling overlapped signals through back propagation neural network, Mechanical Systems and Signal Processing, 231: 112724, https://doi.org/10.1016/j.ymssp.2025.112724.
- Liu F., Cai F., Peng S., Hao R., Ke M., Liu Z. (2009), Parallel acoustic near-field microscope: A steel slab with a periodic array of slits, *Physics Review E*, 80(2): 026603, https://doi.org/10.1103/PhysRevE.80. 026603.

- 24. Liu Z., Lee H., Xiong Y., Sun C., Zhang X. (2007), Far-field optical hyperlens magnifying sub-diffraction-limited objects, *Science*, **315**(5819): 1686, https://doi.org/10.1126/science.1137368.
- 25. Lorenzo A. et al. (2021), Holey-structured tungsten metamaterials for broadband ultrasonic subwavelength imaging in water, The Journal of the Acoustical Society of America, 150(1): 74–81, https://doi.org/10.1121/10.0005483.
- Molerón M., Daraio C. (2015), Acoustic metamaterial for subwavelength edge detection, *Nature Communications*, 6(8): 8037, https://doi.org/10.1038/ncomms 9037.
- 27. Pendry J.B. (2000), Negative refraction makes a perfect lens, *Physical Review Letters*, **85**(18): 3966–3969, https://doi.org/10.1103/PhysRevLett.85.3966.
- SILVEIRINHA M.G., BELOV P.A., SIMOVSKI C.R. (2008), Ultimate limit of resolution of subwavelength imaging devices formed by metallic rods, *Optics Letters*, 33(15): 1726–1728, https://doi.org/10.1364/OL.33.001726.
- 29. Simonetti F. (2006), Multiple scattering: The key to unravel the subwavelength world from the farfield pattern of a scattered wave, *Physical Review E*,

- **73**(3): 036619, https://doi.org/10.1103/PhysRevE.73. 036619.
- 30. Yan X., Yuan F.-G. (2015), Conversion of evanescent Lamb waves into propagating waves via a narrow aperture edge, *The Journal of the Acoustical Society of America*, **137**(6): 3523–3533, https://doi.org/10.1121/1.4921599.
- 31. Zhang S., Yin L., Fang N. (2009), Focusing ultrasound with an acoustic metamaterial network, *Physical Review Letters*, **102**(19): 194301, https://doi.org/10.1103/PhysRevLett.102.194301.
- 32. Zhou Y. et al. (2010), Acoustic surface evanescent wave and its dominant contribution to extraordinary acoustic transmission and collimation of sound, *Physical Review Letters*, **104**(16): 164301, https://doi.org/10.1103/PhysRevLett.104.164301.
- 33. Zhu J. et al. (2010), A holey-structured metamaterial for acoustic deep-subwavelength imaging, Nature Physics, 7(1): 52–55, https://doi.org/10.1038/nphys 1804.
- 34. Zhu X.-F., Wei Q., Wu D.-J., Liu X.-J. (2018), Broadband acoustic subwavelength imaging by rapidly modulated stratified media, *Scientific Reports*, **8**(1): 4934, https://doi.org/10.1038/s41598-018-23411-5.